AC-FPSK modulation for low-energy and low data rate optical wireless communications

Muhammad Jehangir Khan, Ali Waqar Azim, Yannis Le Guennec, G. Maury, Laurent Ros

AC-FPSK Modulation for Low-Energy and Low Data Rate Optical Wireless Communications**

Muhammad Jehangir Khan[a,*], Ali Waqar Azim[b], Yannis Le Guennec[a], Ghislaine Maury[c], Laurent Ros[a]

[a] *Université Grenoble Alpes; CNRS, Grenoble INP, GIPSA-LAB, 38000 Grenoble, France.*
[b] *Department of Telecommunication Engineering, University of Engineering and Technology, 47050 Taxila, Pakistan.*
[c] *Université Grenoble Alpes; Institute of Engineering, Grenoble INP, IMEP-LAHC, 38000 Grenoble, France.*

Abstract

This article proposes an amalgam of phase-shift keying and asymmetrically clipped frequency-shift keying (i.e., AC-FPSK) for low-energy/low-data rate optical wireless communications. We design a near-optimal, low-complexity harmonic receiver by analyzing the AC-FPSK time-domain (TD) and frequency-domain (FD) waveforms. The Euclidean distance analysis between AC-FPSK waveform pairs yields lower and upper bounds for theoretical bit error probability. Using numerical simulations, we present an exhaustive evaluation of the optimal cardinality of PSK, which illustrates the superiority of AC-FPSK. We show that AC-FPSK provides better energy efficiency versus spectral efficiency trade-off than state-of-the-art AC-FSK, direct current-FPSK, pulse amplitude modulation, and asymmetrically clipped optical orthogonal frequency division multiplexing. We also demonstrate that by making a suitable choice for the cardinality of PSK, the proposed 2-tap harmonic receiver for AC-FPSK can reach a similar complexity as the AC-FSK harmonic receiver.

Keywords: Optical wireless communications, frequency-shift keying, phase-shift keying, intensity modulation and direct detection, energy efficient modulation.

1. Introduction

The radio-frequency (RF) spectrum scarcity is a critical issue in Internet of Things (IoT) connectivity despite the fact that the data rate per device generally does not exceed 1 Mbit/s [2]. To mitigate the RF spectrum congestion, optical wireless communication (OWC) is touted as a complementary technology as it offers unlimited un-licenced bandwidth, secure communications, no

*Corresponding author. Tel./fax: +33-751-041-910
Email addresses: Muhammad-Jehangir.Khan@gipsa-lab.grenoble-inp.fr (Muhammad Jehangir Khan), aliwaqarazim@gmail.com (Ali Waqar Azim), yannis.leguennec@gipsa-lab.grenoble-inp.fr (Yannis Le Guennec), ghislaine.maury@grenoble-inp.fr (Ghislaine Maury), laurent.ros@gipsa-lab.grenoble-inp.fr (Laurent Ros)

[**]This paper is a complementary work of our conference paper [1] presented at the 16th International Conference on Signal Processing and Communication System (ICSPCS) in Bydgoszcz, Poland (September 2023).

interference with RF bands, possible concurrent communication and illumination functionalities [3]. Besides these benefits, the omnipresence of low-cost light-emitting diode (LED) lighting infrastructures allows a cheap and non-invasive upgrade for OWC connectivity. OWC systems usually employ simple intensity modulation and direct detection (IM/DD) to transmit and detect the information. For IM/DD, the transmitted signal should be real-valued and non-negative [4] to IM the current of the light source. In the recent past, significant research has been carried out regarding waveform design for high data-rate OWC systems. Since the available bandwidth is limited by the light source and/or by the channel frequency responses, modulation waveforms with high spectral efficiency have been investigated such as optical-orthogonal frequency-division multiplexing (O-OFDM) [5–7] and pulse-amplitude modulation (PAM) [8, 9]. However, these modulations are power-hungry (i.e., with low energy efficiency) and may not be appropriate choices for ultra-reliable energy-efficient (i.e., "low energy") low data rate communications, as they negatively impact the battery-powered user terminals for IoT communications. O-OFDM and PAM waveform belong to the class of linear modulations, for which spectral efficiency increases and energy efficiency decreases with an increase in the modulation order. Hence, the energy efficiency of linear modulations is upper bounded by 2-PAM (i.e., On-Off-Keying (OOK) modulation). On the other hand, using non-linear modulations, it is possible to outperform the energy efficiency of the OOK by increasing the modulation order. This behaviour of the non-linear modulations makes it attractive to target energy-efficient wireless communications [10, 11]. The first waveform design, belonging to the class of orthogonal non-linear modulations, which has been extensively studied for OWC, is pulse-position modulation (PPM) [12–15]. Unfortunately, PPM has some severe limitations for OWC, such as (i) synchronization issues at the receiver; (ii) strong multi-path channel impact on bit error rate (BER) performance; and (iii) high peak to average power ratio (PAPR) [15]. IM/DD consistent frequency-shift keying (FSK) schemes circumvent the above-mentioned limitations of PPM [16–21]. In [16], an asymmetric FSK (AFSK) technique is presented for Visible Light Communications (VLC), but only 2 modulation states are considered for the performance evaluation. In [17], a robust OOK-M-FSK modulation technique is practically implemented without affecting the dimming characteristics of the LED. In [18], a low complexity demodulation strategy for flickering-free M-FSK VLC is proposed using Hamming autocorrelation function. In [19], direct-current (DC)-FSK and unipolar (U)-FSK have been investigated for unipolar generation of FSK-based modulations and in [20, 22], an asymmetrically clipped (AC)-FSK modulation scheme is proposed and shows better energy efficiency than DC-FSK and U-FSK. A low-complexity harmonic receiver has been proposed for AC-FSK in [20], based on frequency-domain cross-correlation computation. In [21], phase-shift keying (PSK) and DC-FSK are amalgamated, resulting in a hybrid frequency and phase-shift keying approach, and is referred to as DC-FPSK. The concept of hybrid modulation is to combine linear and orthogonal modulation properties to increase the spectral efficiency of the initial orthogonal modulation. It is demonstrated in [21] that DC-FPSK outperforms DC-FSK in terms of energy efficiency and spectral efficiency trade-off. In [1], DC-FPSK combined with a very low complexity convolutional code at the transmitter side, and a turbo-decoder (i.e., BCJR algorithm) is adopted at the receiver side, generating turbo-DC-FPSK. Simulations confirmed that turbo-DC-FPSK outperforms DC-FPSK

in terms of energy efficiency and spectral efficiency trade-off.

Against the given background, the contributions of this article are as follows:

1. We propose a hybrid frequency and phase-shift keying approach that employs the precept of AC-FSK, i.e., AC-FPSK. It is demonstrated that the proposed AC-FPSK provides better energy efficiency for a given spectral efficiency than AC-FSK, DC-FPSK, PAM and asymmetrically clipped optical (ACO)-OFDM [5]. Additionally, AC-FPSK offers better energy efficiency as compared to PPM when LED dynamic range limitation is taken into account. It shall become apparent that AC-FSPK is the most energy-efficient approach among the considered schemes for low energy/low data rate OWC.
2. We comprehensively elucidate the time-domain (TD) and frequency-domain (FD) AC-FPSK waveform leading to the development of a near-optimal, low-complexity harmonic receiver for AC-FPSK.
3. The Euclidean distance analysis between AC-FPSK waveform is realized for upper and lower bounds derivation of the AC-FPSK theoretical bit error probability.
4. Using numerical simulations, we comprehensively analyze the optimal cardinality of PSK which provides the best performance for a given frequency shift of AC-FPSK cardinality. This analysis leads to a numerical study of spectral efficiency versus energy efficiency performance. BER simulation results are compared with state-of-the-art AC-FSK, DC-FPSK, PAM, ACO-OFDM and PPM modulation schemes.

The remainder of the article is organized as follows. Section 2 provides the AC-FPSK framework, which includes explaining AC-FPSK signaling, transmitter architecture, spectral efficiency analysis and Euclidean distance analysis. Section 3 presents three different receiver architectures for AC-FPSK (optimal, sub-optimal and harmonic receivers), including a discussion on receivers' complexity. Section 4 provides the upper and lower bounds on theoretical bit error probability for AC-FPSK. Section 5 provides theoretical and simulation BER results relatively to DC-FPSK, AC-FSK, PAM and ACO-OFDM. Conclusions are rendered in Section 6.

2. AC-FPSK Framework

In the sequel, we use the notation $(M_\perp, M_\phi)$-AC-FPSK for the proposed modulation technique, where $M_\perp$ is the number of frequencies, and M_ϕ is the number of phases. In this section, we present the following in the context of $(M_\perp, M_\phi)$-AC-FPSK: (i) IM/DD consistent AC-FPSK signaling and transmitter design; (ii) mathematical expression of the spectral efficiency of AC-FPSK; and (iii) mathematical expressions of the squared Euclidean distance between waveform pairs of the dictionary.

2.1. AC-FPSK Signaling and Transmitter Design

2.1.1. Time-Domain Waveforms

AC-FPSK symbols are derived from $2M$-FSK symbols (considering only the odd frequencies) with M being the dictionary size, and amalgamating them with a phase shift. We consider $M_\perp$

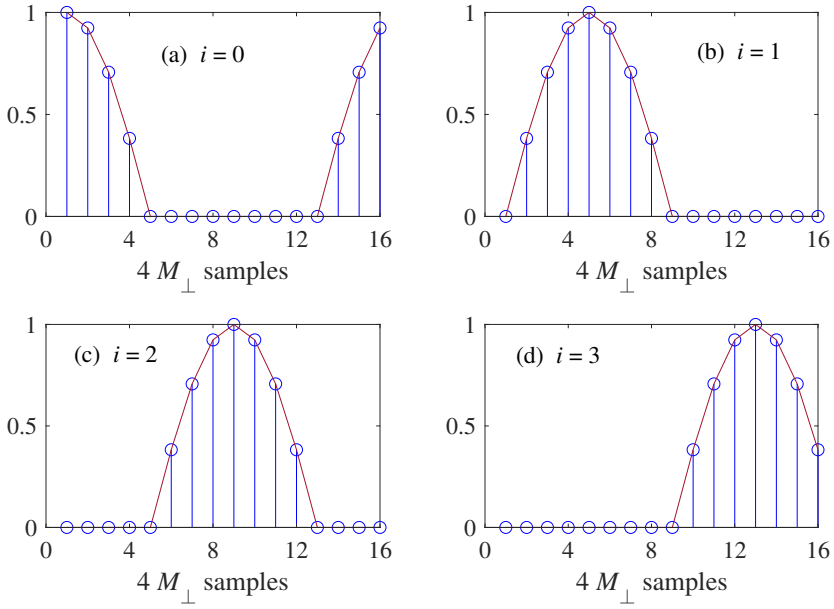

Figure 1: $(M_\perp, M_\phi)$-AC-FPSK TD waveforms for $(M_\perp, M_\phi) = (4, 4)$, with $m = 1$ and $i \in \{0, 1, 2, 3\}$.

orthogonal frequencies, and M_ϕ Gray coded phase shifts, so that the alphabet size of the AC-FPSK modulation is $M = M_\perp \times M_\phi$. The phase shift rotations applied to the complex waveform are given as $z_i = \exp(j\phi_i)$ with $\phi_i = 2\pi i/M_\phi$, and $i \in \{0, 1, \cdots, M_\phi - 1\}$. AC-FPSK waveform can be generated using an inverse discrete Fourier transform (iDFT). For that purpose, we define a Hermitian symmetric FD vector, $\boldsymbol{X}_{m,i}$ that corresponds to the m-th activated frequency and having ϕ_i as phase shift, where $m \in \{1, 2, \cdots, M_\perp\}$, and $i \in \{0, 1, \cdots, M_\phi - 1\}$. Considering that only odd frequencies are used, $\boldsymbol{X}_{m,i}$ is defined as:

$$\boldsymbol{X}_{m,i} = [\underbrace{0}_{\text{DC}}, \underbrace{0, \cdots, 0, z_i, 0, \cdots, 0}_{2M_\perp - 1}, 0, \underbrace{0, \cdots, 0, \overline{z_i}, 0, \cdots, 0}_{2M_\perp - 1}]^{\text{T}}, \tag{1}$$

where $\overline{(\cdot)}$ denotes the complex conjugate. $\boldsymbol{X}_{m,i}$ is of size $M_\text{c} \times 1$, where $M_\text{c} = 4M_\perp$. Note that z_i is located at the index $2m - 1$ in $\boldsymbol{X}_{m,i} = [X[0], \cdots, X[M_\text{c} - 1]]^{\text{T}}$, while $\overline{z_i}$ is located at the index $4M_\perp - 2m + 1$ to incorporate Hermitian symmetry, which is required to produce a real valued signal in time-domain. The discrete time-domain bipolar FPSK waveform, $\boldsymbol{s}_{m,i}^{\text{FPSK}}$, corresponding to $\boldsymbol{X}_{m,i}$, is computed as follows:

$$\boldsymbol{s}_{m,i}^{\text{FPSK}} = \frac{A}{2} \boldsymbol{F}_{M_\text{c}}^{-1} \boldsymbol{X}_{m,i}, \tag{2}$$

where $\boldsymbol{F}_{M_\text{c}}^{-1}$ is the M_c-order iDFT matrix [10] and A is the amplitude of the FPSK waveform. The n-th discrete time sample of the m-th activated frequency and i-th activated phase bipolar FPSK

waveform, $s_{m,i}^{\mathrm{FPSK}}[n]$ is expressed as:

$$\begin{aligned} s_{m,i}^{\mathrm{FPSK}}[n] &= A\cos(2\pi(2m-1)\Delta f(n-1)T_{\mathrm{c}}+\phi_i) \\ n &\in \{1,2,\cdots,M_{\mathrm{c}}\}, \end{aligned} \tag{3}$$

where T_{c} is the chip time, and $\Delta f = 1/T_{\mathrm{s}}$ is the frequency separation between two adjacent waveforms with $T_{\mathrm{s}} = M_{\mathrm{c}}T_{\mathrm{c}}$ the symbol period. This frequency separation ensures the orthogonality between two waveforms, $s_{m,i}^{\mathrm{FPSK}}$ that have distinct values of the index m. The m-th activated frequency and i-th activated phase bipolar FPSK waveform is expressed in a vectorial form as $\boldsymbol{s}_{m,i}^{\mathrm{FPSK}} = \left[s_{m,i}^{\mathrm{FPSK}}[1],\cdots,s_{m,i}^{\mathrm{FPSK}}[M_{\mathrm{c}}]\right]^{\mathrm{T}}$. Unipolar AC-FPSK waveform is generated by clipping the negative samples of bipolar FPSK waveform, $\boldsymbol{s}_{m,i}^{\mathrm{FPSK}}$. The n-th discrete time sample of the m-th activated frequency and i-th activated phase AC-FPSK waveform, $\boldsymbol{s}_{m,i}[n]$ is expressed as:

$$\boldsymbol{s}_{m,i}[n] = \begin{cases} \boldsymbol{s}_{m,i}^{\mathrm{FPSK}}[n] & \boldsymbol{s}_{m,i}^{\mathrm{FPSK}}[n] \geq 0 \\ 0 & \boldsymbol{s}_{m,i}^{\mathrm{FPSK}}[n] < 0 \end{cases}. \tag{4}$$

In the sequel, M AC-FPSK modulation will be referred to as $(M_{\perp}, M_{\phi})$-AC-FPSK. In order to allocate a unique waveform index in the $(M_{\perp}, M_{\phi})$-AC-FPSK dictionary, $\mathcal{D}^{\mathrm{AC-FPSK}}$, an index k is introduced, which depends on m and i as:

$$k = iM_{\perp} + m, \tag{5}$$

with $m \in \{1,2,\cdots,M_{\perp}\}$, $i \in \{0,1,\cdots,M_{\phi}-1\}$ and $k \in \{1,2,\cdots,M\}$, where $M = M_{\perp} \times M_{\phi}$. In the following, AC-FPSK waveform, $\boldsymbol{s}_{m,i}$ will be denoted as $\boldsymbol{s}_k$, corresponding of the k-th waveform in $\mathcal{D}^{\mathrm{AC-FPSK}}$, and defined in vectorial form as $\boldsymbol{s}_k = [\boldsymbol{s}_{m,i}[1],\cdots,\boldsymbol{s}_{m,i}[M_{\mathrm{c}}]]^{\mathrm{T}}$. AC-FPSK dictionary, $\mathcal{D}^{\mathrm{AC-FPSK}}$ is created by interpolating $(M_{\perp}, M_{\phi})$-AC-FPSK waveforms in a look-up table (LUT). The size of $\mathcal{D}^{\mathrm{AC-FPSK}}$ is $M = M_{\perp}M_{\phi}$ and the number of bits per AC-FPSK waveform is $b = b_{\perp}+b_{\phi}$, where $b_{\perp} = \log_2(M_{\perp})$, and $b_{\phi} = \log_2(M_{\phi})$. Fig. 1 depicts the TD illustration of the $(M_{\perp}, M_{\phi})$-AC-FPSK waveforms for $(M_{\perp}, M_{\phi}) = (4,4)$, $m = 1$ and $i \in \{0,1,2,3\}$. All the waveforms, $\boldsymbol{s}_k$ in $\mathcal{D}^{\mathrm{AC-FPSK}}$ have the same electrical symbol energy, $E_{\mathrm{s_{(elec)}}}$ given as:

$$E_{\mathrm{s_{(elec)}}} = \|\boldsymbol{s}_k\|^2 = \frac{A^2}{4}T_{\mathrm{s}}, \tag{6}$$

where $\|\cdot\|$ represents the Euclidean norm.

2.1.2. Frequency-Domain Waveforms

AC-FPSK FD waveforms, $\boldsymbol{S}_k$, are attained by applying M_{c}-order DFT on $\boldsymbol{s}_k$ as:

$$\boldsymbol{S}_k = \boldsymbol{F}_{M_{\mathrm{c}}}\boldsymbol{s}_k, \tag{7}$$

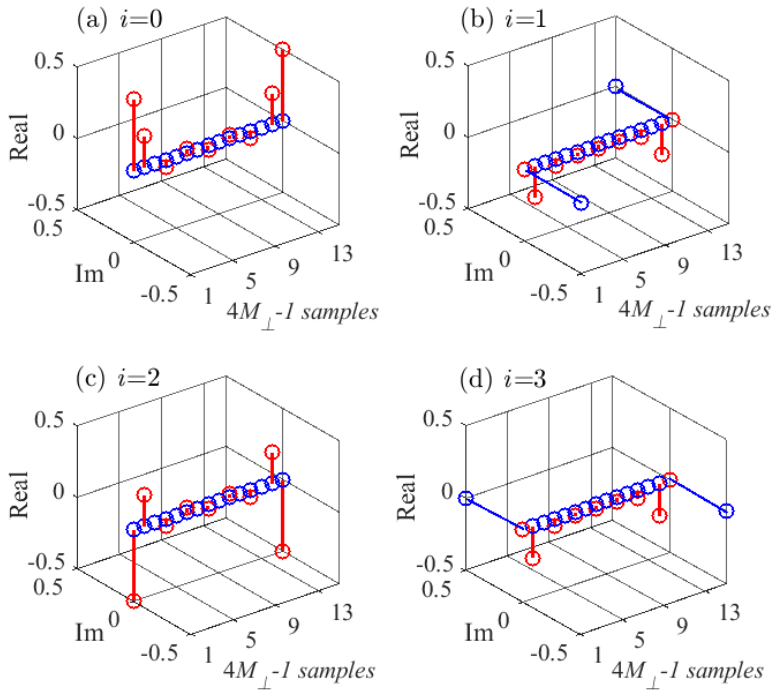

Figure 2: $(M_\perp, M_\phi)$-AC-FPSK FD waveforms for $(M_\perp, M_\phi) = (4, 4)$, $m = 1$ and $i \in \{0, 1, 2, 3\}$. Real part of waveform spectrum is in red and Imaginary (Im) part is in blue.

where $\boldsymbol{F}_{M_c}$ is M_c-order DFT matrix [10].

Fig. 2 illustrates real (in red color) and imaginary parts (in blue color) of $(M_\perp, M_\phi)$-AC-FPSK waveform spectra considering $(M_\perp, M_\phi) = (4, 4)$, $m = 1$ and $i \in \{0, 1, 2, 3\}$. DC spectral components are not illustrated; therefore, the FD waveforms show $4M_\perp$-1 samples. Since AC-FPSK TD waveforms are real, spectra shown in Fig. 2 depict Hermitian symmetry. Moreover, from Fig. 2, it can be seen that a limited number of real and imaginary spectral components (i.e., taps) have significant amplitudes. Irrespective of $(M_\perp, M_\phi)$, we have estimated that only four taps (excluding the DC component), for real and imaginary spectra altogether, contain more than 99% of the AC-FPSK symbol energy. The result shown in Fig. 2 is in-line with [20], in which a single phase $\phi = 0$ is considered, and inverse discrete cosine transform (iDCT) is used to generate AC-FSK waveforms, leading to waveform spectrum (using DCT) without Hermitian symmetry property. As a result, only two taps contain 99% of the symbol energy for AC-FSK FD waveforms, while four taps contain 99% of the symbol energy for AC-FPSK FD waveforms.

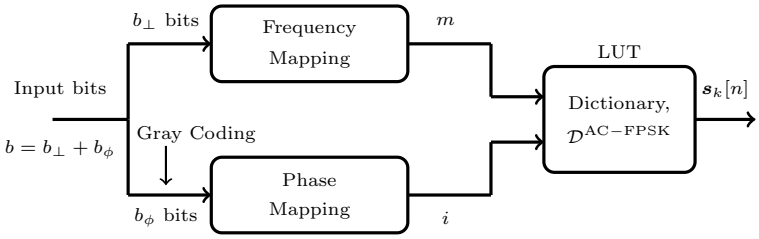

Figure 3: Transmitter configuration of $(M_\perp, M_\phi)$-AC-FPSK.

Table 1: Comparison between spectral efficiencies of M AC-FSK, $(M_\perp, M_\phi)$-DC-FPSK and $(M_\perp, M_\phi)$-AC-FPSK. Here $M = M_\perp \times M_\phi$ with $M_\phi = 1$ for M AC-FSK.

Modulation Scheme	η
M AC-FSK	$\frac{\log_2(M)}{M}$
$(M_\perp, M_\phi)$-DC-FPSK	$M_\phi \times \frac{\log_2(M)}{M}$
$(M_\perp, M_\phi)$-AC-FPSK	$M_\phi \times \frac{\log_2(M)}{2M}$

2.1.3. AC-FPSK Transmitter Design

Fig. 3 illustrates the transmitter configuration for $(M_\perp, M_\phi)$-AC-FPSK, where the m-th frequency is chosen using $b_\perp$ bits, and the i-th phase shift is chosen considering b_ϕ bits. $\{m; i\}$ identifies the waveform index k (5), to generate $\boldsymbol{s}_k$ from a LUT that contains the dictionary $\mathcal{D}^{\text{AC-FPSK}}$.

2.2. AC-FPSK Spectral Efficiency

Since $(M_\perp, M_\phi)$-AC-FPSK transmits $b = b_\perp + b_\phi$ bits per waveform, bit rate, R_b is $R_\text{b} = b/T_\text{s}$. Moreover, $(M_\perp, M_\phi)$-AC-FPSK occupies bandwidth equal to $B \approx 2M_\perp \Delta f = 2M_\perp/T_\text{s}$ (neglecting the out-of-band harmonics generated by clipping [20]). Consequently, $(M_\perp, M_\phi)$-AC-FPSK spectral efficiency, η can be expressed as:

$$\eta = \frac{R_b}{B} = \frac{\log_2(M_\perp M_\phi)}{2M_\perp}. \tag{8}$$

Eq. (8) suggests that η increases by increasing the number of phases, M_ϕ, while keeping $M_\perp$ constant (as for a linear modulation). On the other hand, η decreases by increasing $M_\perp$, while keeping M_ϕ constant (as for an orthogonal modulation). Table 1 summarizes the spectral efficiencies of the conventional M AC-FSK [20], $(M_\perp, M_\phi)$-DC-FPSK [21], and the proposed $(M_\perp, M_\phi)$-AC-FPSK for the same modulation order, $M = M_\perp \times M_\phi$. It can be noticed from Table 1 that the spectral efficiency of $(M_\perp, M_\phi)$-AC-FPSK increases by M_ϕ compared to the spectral efficiency of M AC-FSK due to the use of additional phase shifts. However, it is decreased by a factor 2 due to the use of iDFT for AC-FPSK generation instead of iDCT as in the case of AC-FSK

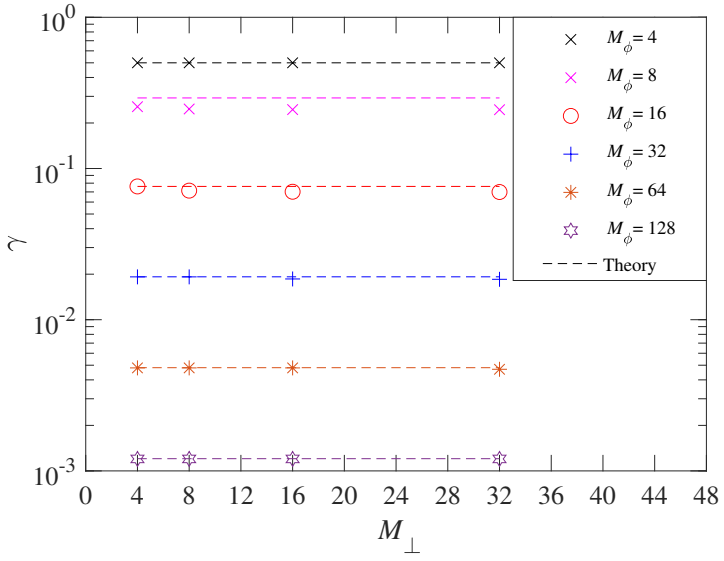

Figure 4: Simulation of γ with respect to $M_\phi \geq 8$ considering different $M_\perp$ for $(M_\perp, M_\phi)$-AC-FPSK. Theoretical approximation for γ in (13) is reported using dash-line for each M_ϕ.

waveform generation. It may be noticed that the spectral separation between adjacent frequency tones is double for iDFT (i.e., $\Delta f = 1/T_\mathrm{s}$ [21]) relative to DCT (i.e., $\Delta f = 1/2T_\mathrm{s}$ [19]) to maintain orthogonality between the (phase-shifted) discrete frequency tones. Table 1 also shows that the spectral efficiency of $(M_\perp, M_\phi)$-AC-FPSK is half the spectral efficiency of $(M_\perp, M_\phi)$-DC-FPSK for the same modulation order, due to the use of only odd frequencies to generate AC-FPSK waveforms.

2.3. Euclidean Distance between AC-FPSK Symbols

The squared Euclidean distance, $d^2_{k,k'}$ between any waveform pair $\{\boldsymbol{s}_k; \boldsymbol{s}_{k'}\}$, $k \neq k'$ in AC-FPSK dictionary can be evaluated as [21]:

$$\begin{aligned} d^2_{k,k'} &= \|\boldsymbol{s}_k - \boldsymbol{s}_{k'}\|^2 \\ &= 2E_{\mathrm{s(elec)}} - 2\langle \boldsymbol{s}_k, \boldsymbol{s}_{k'} \rangle. \end{aligned} \tag{9}$$

To find the minimum squared Euclidean distance, $d^2_{\min}$ between waveform pairs, $\{\boldsymbol{s}_k; \boldsymbol{s}_{k'}\}$, we determine the maximum inner product $\langle \boldsymbol{s}_k, \boldsymbol{s}_{k'} \rangle_{\max}$ in (9). It is highlighted that the inner product $\langle \boldsymbol{s}_k, \boldsymbol{s}_{k'} \rangle$ between any pair of waveform in $\mathcal{D}^{\mathrm{AC-FPSK}}$ is not null, because AC-FPSK waveform are no longer orthogonal to each other due to the clipping process [20]. Therefore, it is viable to define an upper bound for $\langle \boldsymbol{s}_k, \boldsymbol{s}_{k'} \rangle$, leading to $d^2_{\min}$ by using (9). Through simulations, it is found that

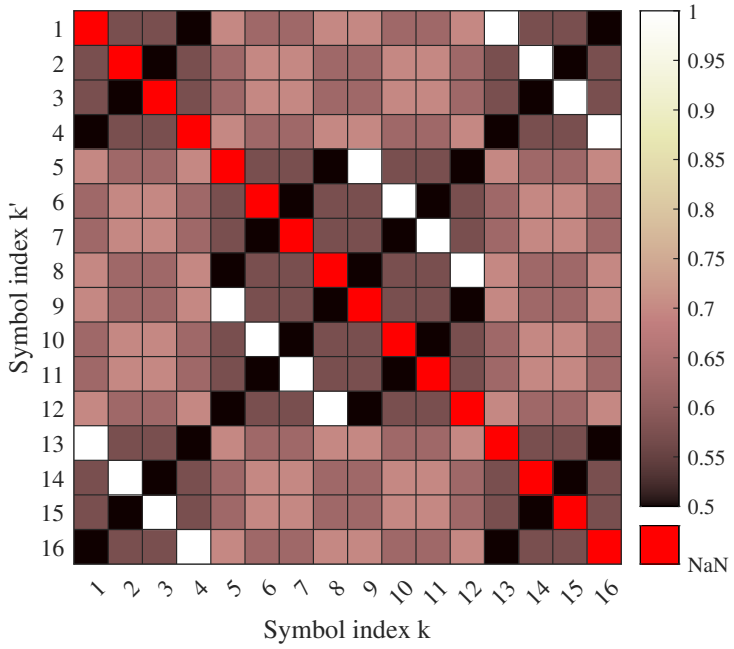

Figure 5: Normalized squared Euclidean distance between $\boldsymbol{s}_k$ and $\boldsymbol{s}_{k'}$, $d_{k,k'}/2E_{\mathrm{s}_{(\mathrm{elec})}}$ for $k \neq k'$. NaN: Not a Number.

the maximum inner product $\langle \boldsymbol{s}_k, \boldsymbol{s}_{k'} \rangle_{\max}$, for $k \neq k'$, can be approximated as:

$$\langle \boldsymbol{s}_k, \boldsymbol{s}_{k'} \rangle_{\max} \approx \begin{cases} 0.5E_{\mathrm{s(elec)}} & \text{for } M_\phi = 2, 4 \\ 2E_{\mathrm{s(elec)}} \cos\left(\frac{2\pi}{M_\phi}\right) & \text{for } M_\phi \geq 8 \end{cases}. \tag{10}$$

By incorporating (10) in (9), $d^2_{\min}$ is expressed as:

$$d^2_{\min} \approx \begin{cases} E_{\mathrm{s(elec)}} & \text{for } M_\phi = 2, 4 \\ 2E_{\mathrm{s(elec)}} \left[1 - \cos\left(\frac{2\pi}{M_\phi}\right)\right] & \text{for } M_\phi \geq 8 \end{cases}. \tag{11}$$

From (11), $d^2_{\min}$ can be simplified as:

$$d^2_{\min} = 2\gamma E_{\mathrm{s}_{(\mathrm{elec})}}, \tag{12}$$

where γ is the penalty factor on the minimum squared Euclidean distance induced by the loss of orthogonality ($\gamma = 1$ for conventional FSK modulation [19]) and is given as:

$$\gamma \approx \begin{cases} 0.5 & \text{for } M_\phi = 2, 4 \\ 1 - \cos\left(\frac{2\pi}{M_\phi}\right) & \text{for } M_\phi \geq 8 \end{cases}. \tag{13}$$

Fig. 4 depicts simulation results for γ from $\langle \boldsymbol{s}_k, \boldsymbol{s}_{k'} \rangle_{\max}$ numerical computation and approximated γ evaluation from (13) for $M_\phi \in \{4, 8, \cdots, 128\}$ and $M_\perp \in \{4, 8, \cdots, 32\}$. It can be observed from Fig. 4 that γ is independent from $M_\perp$, which is in-line with the theoretical approximation of Eq. (13). Fig. 5 represents a heat-map of the normalized squared Euclidean distance, $d^2_{k,k'}/2E_{\mathrm{s(elec)}}$ between $\boldsymbol{s}_k$ and $\boldsymbol{s}_{k'}$ for (4, 4)-AC-FPSK. It can be observed from Fig. 5 that $d^2_{\min}/2E_{\mathrm{s(elec)}} = \gamma = 0.5$, which is in-line with (13). Moreover, it can be seen that, for any AC-FPSK waveform $\boldsymbol{s}_k$, $d^2_{\min}/2E_{\mathrm{s(elec)}}$ is reached only with 2 neighboured waveforms, $\boldsymbol{s}_{k'}$ (i.e., 2 black boxes per column in Fig. 5). It means that, for any AC-FPSK waveform, only 2 neighboured waveforms are at an Euclidean distance corresponding to the minimum Euclidean distance, $d_{\min}$.

3. AC-FPSK Receivers

The received waveform, $\boldsymbol{r}$ contaminated by the ambient noise, $\boldsymbol{n}$ is given as:

$$\boldsymbol{r} = \boldsymbol{s}_{m,i} + \boldsymbol{n}, \tag{14}$$

where $\boldsymbol{n}$ is an additive white Gaussian noise (AWGN) having a mono-lateral power spectral density (PSD) of N_0. For clarity of exposition, $\boldsymbol{n}$ and $\boldsymbol{r}$ in vectorial forms are given as $\boldsymbol{n} = [n[1], \cdots, n[M_{\mathrm{c}}]]^{\mathrm{T}}$ and $\boldsymbol{r} = [r[1], \cdots, r[M_{\mathrm{c}}]]^{\mathrm{T}}$.

3.1. Optimal time-domain ML receiver

The receiver architecture for the optimal TD ML receiver for $(M_\perp, M_\phi)$-AC-FPSK is illustrated in Fig. 6 (red/black). Since all AC-FPSK waveforms, $\boldsymbol{s}_k$ in the dictionary, $\mathcal{D}^{\mathrm{AC-FPSK}}$ have identical electrical symbol energy, $E_{\mathrm{s(elec)}}$, and considering the equal probability of transmit waveforms, i.e., $p(\boldsymbol{s}_k) = 1/M_\perp M_\phi$, the optimal TD ML receiver identifies $\boldsymbol{s}_k$ in the dictionary, $\mathcal{D}^{\mathrm{AC-FPSK}}$ by maximizing the likelihood function, $p(\boldsymbol{r}|\boldsymbol{s}_k)$ [21]. Here $p(\boldsymbol{r}|\boldsymbol{s}_k)$ is the conditional probability density function of receiving $\boldsymbol{r}$ when $\boldsymbol{s}_k$ is transmitted. Considering an AWGN channel having noise variance $\sigma^2 = N_o B$, the likelihood function is given as [21]:

$$\begin{aligned} p(\boldsymbol{r}|\boldsymbol{s}_k) &= \left(\frac{1}{2\pi\sigma^2}\right)^{M_{\mathrm{c}}} \exp\left(-\frac{\|\boldsymbol{r} - \boldsymbol{s}_k\|^2}{2\sigma^2}\right) \\ &= \Gamma \exp\left(\frac{\langle \boldsymbol{r}, \boldsymbol{s}_k \rangle}{\sigma^2}\right), \end{aligned} \tag{15}$$

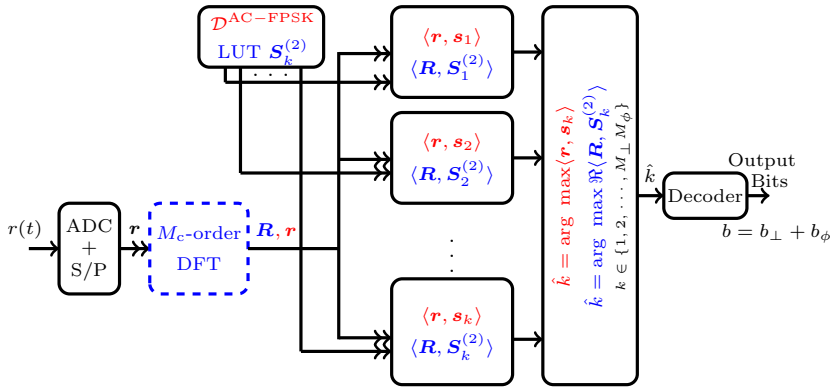

Figure 6: Optimal TD ML receiver (red/black) and 2-tap harmonic receiver (blue/black) architecture for $(M_\perp, M_\phi)$-AC-FPSK.

where $\Gamma = (1/2\pi\sigma^2)^{M_c} \exp(-(\|\boldsymbol{r}\|^2 + \|\boldsymbol{s}_k\|^2)/2\sigma^2)$, while $\|\boldsymbol{r} - \boldsymbol{s}_k\|^2 = \|\boldsymbol{r}\|^2 + \|\boldsymbol{s}_k\|^2 - 2\langle \boldsymbol{r}, \boldsymbol{s}_k \rangle$. Note that $\|\boldsymbol{r}\|^2$ and $\|\boldsymbol{s}_k\|^2 = E_{\mathrm{s(elec)}}$ are constant for any $k \in \{1, 2, \cdots, M_\perp M_\phi\}$. Therefore, the TD ML receiver identifies the symbol index, $\hat{k}$ that maximizes the TD cross-correlation between $\boldsymbol{r}$ and $\boldsymbol{s_k} \in \boldsymbol{\mathcal{D}}^{\mathrm{AC-FPSK}}$ as:

$$\hat{k} = \arg \max_k \langle \boldsymbol{r}, \boldsymbol{s}_k \rangle, \quad k \in \{1, 2, \cdots, M_\perp M_\phi\}. \tag{16}$$

The Fourier transform ensures the inner product preservation, thanks to the Plancherel-Parseval theorem (with a real valued result in our case). As a consequence, the symbol index, $\hat{k}$ can be also identified through the FD cross-correlation as:

$$\hat{k} = \arg \max_k \Big\{ \langle \boldsymbol{R}, \boldsymbol{S}_k \rangle \Big\}, \quad k \in \{1, 2, \cdots, M_\perp M_\phi\}. \tag{17}$$

where $\boldsymbol{R}$ is the M_c-order DFT of $\boldsymbol{r}$, and $\boldsymbol{S}_k$ are the AC-FPSK FD waveforms. The computational complexity of the FD ML receiver increases comparatively to the TD ML receiver, due to the additional M_c-order DFT operation together with the FD cross-correlations. Since the FD ML receiver shows a larger complexity than the TD ML receiver, it will not be considered in the following.

3.2. Sub-optimal (1-tap DFT) Receiver

The sub-optimal (1-tap DFT) receiver structure for $(M_\perp, M_\phi)$-AC-FPSK is illustrated in Fig. 7. As a first step, M_c-order DFT of $\boldsymbol{r}$ is computed as:

$$\boldsymbol{R} = \boldsymbol{F}_{M_c} \boldsymbol{r}, \tag{18}$$

where $\boldsymbol{F}_{M_c}$ is the M_c-order DFT matrix and $\boldsymbol{R} = [R[1], \cdots, R[M_c]]^{\mathrm{T}}$. Afterward, the decision is taken on a single tap per sub-carrier, having maximum amplitude to identify the activated frequency

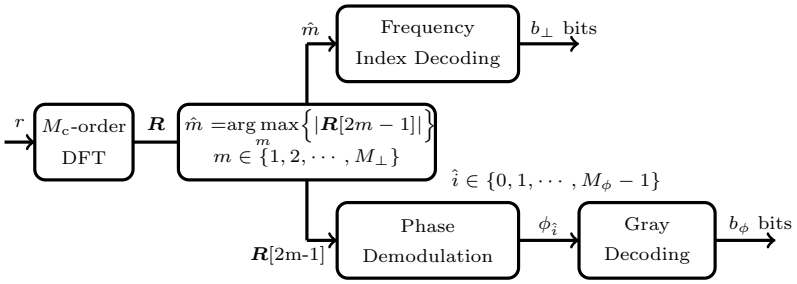

Figure 7: Sub-optimal 1-tap DFT receiver architecture for $(M_\perp, M_\phi)$-AC-FPSK.

index, m as:

$$\hat{m} = \arg\max_m \left\{|\boldsymbol{R}[2m-1]|\right\}, \quad m \in \{1, 2, \cdots, M\}, \tag{19}$$

where $\boldsymbol{R}[2m-1]$ represents the M_c-order DFT of $\boldsymbol{r}$ evaluated at the odd frequency index $2m-1$. Note that frequency index identification is realized only on the first $M_c/2$ samples of $\boldsymbol{R}$ because of the Hermitian symmetry. The estimated phase index $\hat{i}$, is identified using phase demodulation on $\boldsymbol{R}[2\hat{m}-1]$. Finally, decoding of $\hat{m}$ and $\hat{i}$ is operated to define the output bits.

3.3. 2-tap Harmonic receiver

Extending the work of [20], harmonic receiver evaluates the cross-correlation of the FD received waveform, $\boldsymbol{R}$ with a limited number, L, of components (i.e., taps) from the AC-FPSK FD waveforms, with $L < M_c$. By analyzing the $(M_\perp, M_\phi)$-AC-FPSK FD waveforms (cf. Fig. 2), we have shown that the waveform spectrum exhibits Hermitian symmetry property and that four taps contain 99% of the symbol energy. However, since the noise at receiver input is also a real signal, FD cross-correlation between the received FD waveform and the AC-FPSK FD waveforms can be computed only over the first $M_c/2$ chips, without any penalty on signal-to-noise ratio at the FD correlator output. Fig. 6 in (blue/black) illustrates the harmonic receiver architecture for $(M_\perp, M_\phi)$-AC-FPSK. In a first step (off-line step to do only once), the two most significant taps over the first $M_c/2$ chips of AC-FPSK FD waveforms (leaving aside the DC component) are selected. The other samples are forced to zero, to build a dictionary of M $\boldsymbol{S}_k^{(2)}$ waveforms, that are then interpolated in a LUT. In a second step (on-line step to do at symbol rate), M_c-order DFT is applied on $\boldsymbol{r}$ to obtain $\boldsymbol{R}$ as in (18). Lastly, the FD cross-correlation is evaluated between $\boldsymbol{R}$ and $\boldsymbol{S}_k^{(2)}$ to identify the transmit frequency index, $\hat{k}$ as:

$$\hat{k} = \arg\max_k \Re\langle \boldsymbol{R}, \boldsymbol{S}_k^{(2)} \rangle, \qquad k \in \{1, 2, \cdots, M_\perp M_\phi\}. \tag{20}$$

where $\Re$ is the real part operator. Here, real part selection is necessary because weak values of imaginary parts emerge from the FD cross-correlations (20), which is due to the derivation of $\boldsymbol{S}_k^{(2)}$ that integrates only the 2 most significant taps of $\boldsymbol{S}_k$ and discards the others.

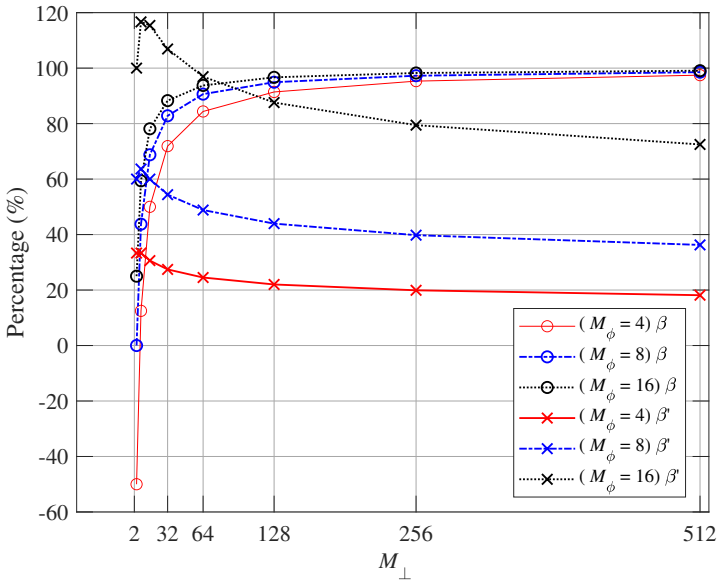

Figure 8: Percentage (%) of complexity reduction, β for 2-tap harmonic receiver relative to the optimal TD ML receiver and percentage of complexity overhead, β' for 2-tap harmonic receiver relative to the 1-tap DFT receiver for $(M_\perp, M_\phi)$-AC-FPSK, considering different $M_\perp$ and M_ϕ.

3.4. AC-FPSK Receiver Complexity Analysis

It can be noticed that the major contributor in receiver complexity is the number of non-zero multiplications [22].

3.4.1. TD ML receiver complexity

There are $(M = M_\perp M_\phi)$ waveforms in the dictionary, $\mathcal{D}^{\mathrm{AC-FPSK}}$ and each waveform consists of $M_\mathrm{c} = 4M_\perp$ chips with half of the chips clipped to zero. The optimal TD ML receiver realizes M TD cross-correlations between the received signal, $\boldsymbol{r}$ and the dictionary waveforms, so it requires $\mathcal{C}_{\mathrm{TDML}} = 2M_\perp^2 M_\phi$ non-zero real multiplications.

3.4.2. 1-tap DFT receiver complexity

We assume that the Fast Fourier transform (FFT) algorithm is used to implement the 1-tap DFT receiver, therefore, it requires $8M_\perp \log_2(4M_\perp)$ real multiplications. After FFT computation and frequency index identification, phase demodulation is performed, which requires additional $4M_\phi$ real multiplications. As a result, the overall complexity for the 1-tap DFT receiver is $\mathcal{C}_{1-\mathrm{tap}} = 8M_\perp \log_2(4M_\perp) + 4M_\phi$.

3.4.3. 2-tap harmonic receiver complexity

The 2-tap harmonic receiver is also based on M_c-order DFT as initial stage, followed by $M = M_\perp M_\phi$ FD cross-correlations. For each FD correlation, 2 complex chips from DFT mul-

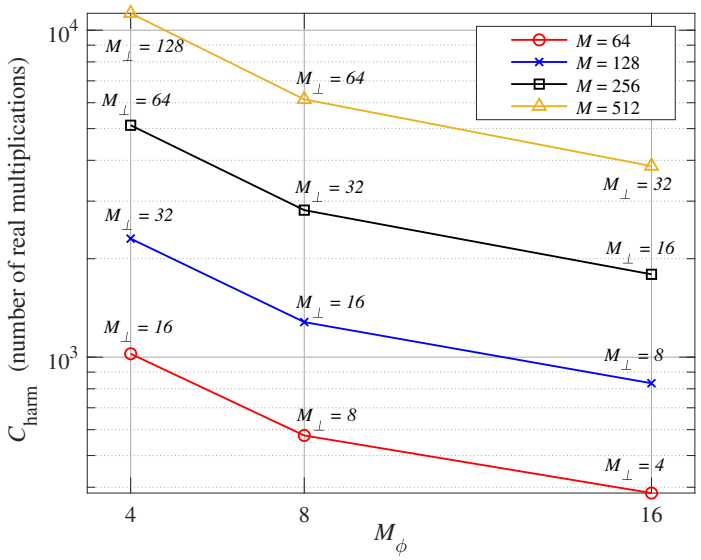

Figure 9: Complexity of 2-tap harmonic receiver for $(M_\perp, M_\phi)$-AC-FPSK, $\mathcal{C}_{\text{harm}}$ for different modulation orders $M = M_\perp \times M_\phi$, varying M_ϕ and $M_\perp$.

tiply with 2-taps (real or imaginary), which leads to a total of $4M_\perp M_\phi$ multiplications for $M_\perp M_\phi$ FD correlations. As a result, the overall complexity for the 2-tap harmonic receiver is $\mathcal{C}_{\text{harm}} = 8M_\perp \log_2(4M_\perp) + 4M_\perp M_\phi$.

Fig. 8 presents the complexity variation parameters, $\beta = (1 - \mathcal{C}_{\text{harm}}/\mathcal{C}_{\text{TDML}}) \times 100\%$ and $\beta' = (\mathcal{C}_{\text{harm}}/\mathcal{C}_{1-\text{tap}} - 1) \times 100\%$, that compute the complexity reduction of the 2-tap harmonic receiver as compared to the optimal TD ML receiver and the complexity overhead of the 2-tap harmonic receiver as compared to the 1-tap DFT receiver, respectively, for different $M_\perp$ and M_ϕ. From Fig. 8, it can be seen that the complexity of the harmonic receiver is drastically reduced compared to the TD ML receiver. This complexity reduction is almost 95% for $M_\perp = 512$ irrespective of M_ϕ. It can also be seen from Fig. 8 that the complexity overhead of the harmonic receiver relatively to the 1-tap DFT receiver is moderate: not more than 40% complexity overhead for $M_\perp = 512$ and $M_\phi \leq 8$.

Fig. 9 shows the evolution of the AC-FPSK 2-tap harmonic receiver complexity for different alphabet cardinalities, $M = M_\perp M_\phi$, as a function of $M_\perp$ and M_ϕ. As shown from Fig. 9, for a given M, the 2-tap harmonic receiver complexity can be reduced by increasing M_ϕ. Indeed, by increasing M_ϕ, for a fixed $M = M_\perp M_\phi$, $M_\perp$ is reduced, leading a reduction of the DFT order (and related FFT order). Since FFT computation has the largest contribution to the harmonic receiver complexity, increasing M_ϕ leads to a decrease in the overall 2-tap harmonic receiver complexity.

4. Bit Error Probability for AC-FPSK

The theoretical bit error probability expression for ML detection of conventional M FSK in AWGN channel is well known and demonstrated in [10]. It is a function of the minimum squared Euclidean distance between FSK waveforms, $d^2_{\text{min,FSK}}$ which is equal to the distance between any FSK waveform pairs, due to the orthogonality property.

4.1. Upper bound for Theoretical Bit Error Probability

In Section 2.3, we have approximated the minimum squared Euclidean distance between any pair of AC-FPSK waveforms, d^2_{min} (12). Supposing that the squared Euclidean distance between any AC-FPSK waveform pair is d^2_{min}, an upper bound for the AC-FPSK bit error probability, P_{e}^{ub} can be easily obtained by substituting $d^2_{\text{min,FSK}}$ with d^2_{min} found for AC-FPSK (12) in the FSK bit error probability expression [10], which leads to:

$$\begin{aligned} P_{\text{e}}^{\text{ub}} =& \frac{M}{2\sqrt{2\pi}(M-1)} \int_{-\infty}^{+\infty} \left[1-(1-Q(x))^{M-1}\right] \\ & \times \exp\left(-\frac{1}{2}\left(x-\sqrt{2\frac{E_{\text{s(elec)}}}{N_0}\gamma}\right)^2\right)\text{d}x, \end{aligned} \tag{21}$$

where $Q(\cdot)$ is the Gaussian Q-function [10], $M = M_{\perp} \times M_{\phi}$ and $E_{\text{s(elec)}} = \log_2(M)E_{\text{b(elec)}}$, $E_{\text{b(elec)}}$ being the average energy per bit. Note that, in Eq. (21), the term $(1-Q(x))^{M-1}$ is related to the contribution of the $M-1$ neighboured waveforms into the bit error probability. All these $M-1$ neighboured waveforms are supposed to be at a squared Euclidean distance d^2_{min}. As a consequence, Eq. (21) is an upper bound for AC-FPSK bit error probability since it has been shown in Fig. 5 that only a limited number of AC-FPSK waveform pairs show a squared Euclidean distance equal to d^2_{min}.

4.2. Lower bound for Theoretical Bit Error Probability

Taking into account that only a limited number, N of AC-FPSK waveform pairs show a squared Euclidean distance equal to d^2_{min} (5), a lower bound for the AC-FPSK theoretical bit error probability, P_{e}^{lb} can be derived as:

$$\begin{aligned} P_{\text{e}}^{\text{lb}} =& \frac{M}{2\sqrt{2\pi}(M-1)} \int_{-\infty}^{+\infty} \left[1-(1-Q(x))^{N}\right] \\ & \times \exp\left(-\frac{1}{2}\left(x-\sqrt{2\frac{E_{\text{s(elec)}}}{N_0}\gamma}\right)^2\right)\text{d}x, \end{aligned} \tag{22}$$

where the $(1-Q(x))^N$ term accounts for the contribution of the N closest AC-FPSK neighboured waveforms at squared Euclidean distance d^2_{min}. This time, all neighboured AC-FPSK waveforms located at a squared Euclidean distance larger than d^2_{min} have been neglected in the bit error probability evaluation.

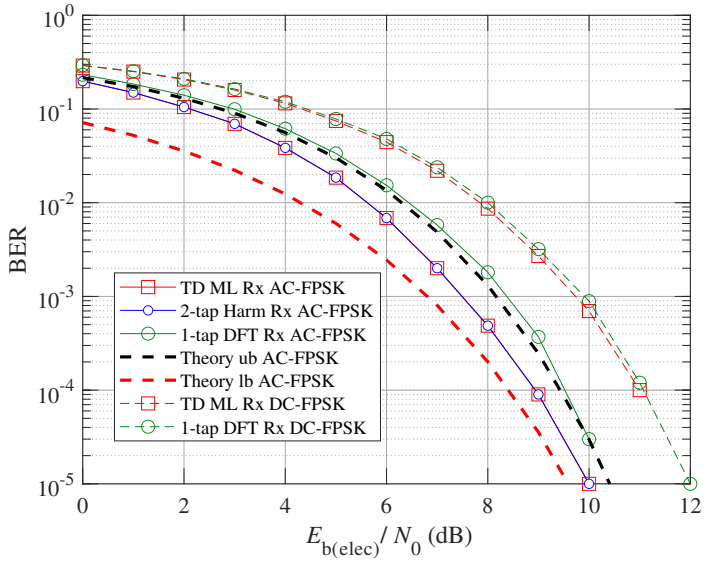

Figure 10: Simulated BER performance against $E_{\mathrm{b(elec)}}/N_0$ for $(M_\perp, M_\phi)$-AC-FPSK versus $(M_\perp, M_\phi)$-DC-FPSK in AWGN channel, considering $M_\perp = 16, M_\phi = 4$. Lower and upper bounds for the AC-FPSK theoretical bit error probability have been reported in dashed lines.

5. Theoretical and Simulation Results

In this section, we present the theoretical and simulation results for the proposed $(M_\perp, M_\phi)$-AC-FPSK scheme, and compare the results with the state-of-the-art $(M_\perp, M_\phi)$-DC-FPSK [21], M AC-FSK [20], M PAM and ACO-OFDM. ACO-OFDM has been considered with low modulation orders here, since it offers one of the best energy efficiency among O-OFDM modulation schemes [7]. For simulation purpose, a Monte-Carlo Matlab model has been developed integrating the AC-FPSK transmitter presented in section 2, the different receivers investigated in section 3, and considering an AWGN channel. Monte Carlo simulation results are averaged over 10^6 separate runs for BER averaging. We evaluate the following performance parameters: (i) BER performance comparison in AWGN channel considering the different receivers for $(M_\perp, M_\phi)$-AC-FPSK; (ii) BER performance comparison in AWGN channel between $(M_\perp, M_\phi)$-AC-FPSK, $(M_\perp, M_\phi)$-DC-FPSK, M AC-FSK, M PAM and ACO-OFDM.

5.1. BER performance comparison between receivers for $(M_\perp, M_\phi)$-AC-FPSK versus $(M_\perp, M_\phi)$-DC-FPSK

Fig. 10 illustrates the simulation results for BER performance against $E_{\mathrm{b(elec)}}/N_0$ (where $E_{\mathrm{b(elec)}} = E_{\mathrm{s(elec)}}/\log_2(M)$) of optimal TD ML receiver, 1-tap DFT receiver and 2-tap harmonic receiver (Harm Rx) for $(M_\perp, M_\phi)$-AC-FPSK and optimal TD ML receiver and 1-tap DFT receiver for $(M_\perp, M_\phi)$-DC-FPSK [21], considering an AWGN channel, $M_\perp = 16$ and $M_\phi = 4$. Theoretical

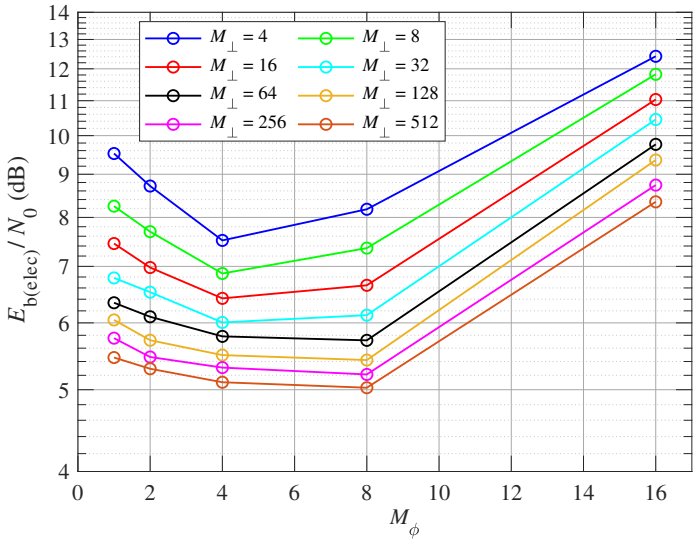

Figure 11: Evaluation of necessary $E_{\mathrm{b(elec)}}/N_0$ to achieve a BER $= 10^{-3}$ for different M_ϕ and $M_\perp$, considering 2-tap harmonic receiver for $(M_\perp, M_\phi)$-AC-FPSK.

upper (21) and lower (22) bounds for the bit error probability have also been reported in Fig. 10, considering that, for any transmitted waveform, the number of neighboured waveforms at squared Euclidean distance $d^2_{\min}$ is $N = 2$ (see Fig. 5). Fig. 10 shows that the optimal TD ML and the 1-tap DFT receivers for $(M_\perp, M_\phi)$-AC-FPSK have around 2 dB improvement in $E_{\mathrm{b(elec)}}/N_0$ relatively to their counterpart for $(M_\perp, M_\phi)$-DC-FPSK, to reach a BER of 10^{-4} . It can also be seen in Fig. 10 that the theoretical lower and upper bounds for the AC-FPSK bit error probability give a relatively accurate range to estimate the bit error probability. For example, for a target BER of 10^{-5}, the $E_{\mathrm{b(elec)}}/N_0$ interval between the lower and upper bounds for bit error probability is of only 1 dB. Furthermore, Fig. 10 reveals that the 2-tap harmonic receiver has exactly the same BER performance as the optimal TD ML receiver for $(M_\perp, M_\phi)$-AC-FPSK, while the 1-tap DFT receiver shows degraded performance of about 0.5 dB in $E_{\mathrm{b(elec)}}/N_0$ to reach a BER of 10^{-4}. In the following sections, we will only consider the 2-tap harmonic receiver for AC-FPSK performance evaluation, since it shows similar performance as the optimal TD ML receiver but with a drastically reduced complexity (see section 3.4).

5.2. Evaluation of Optimum M_ϕ for Energy Efficiency

Fig. 11 illustrates the required $E_{\mathrm{b(elec)}}/N_0$ for $(M_\perp, M_\phi)$-AC-FPSK to target a BER $= 10^{-3}$ for different $M_\perp$ and M_ϕ, considering the 2-tap harmonic receiver. From Fig. 11, it can be observed that the optimum number of phases that minimizes the required $E_{\mathrm{b(elec)}}/N_0$ to reach a BER $= 10^{-3}$ (i.e., which maximises the energy efficiency) is $M_\phi = 4$ when $M_\perp \leq 32$ and is $M_\phi = 8$ when $M_\perp > 32$. However, since the number of phases M_ϕ, impacts the AC-FPSK spectral efficiency (see Table 1),

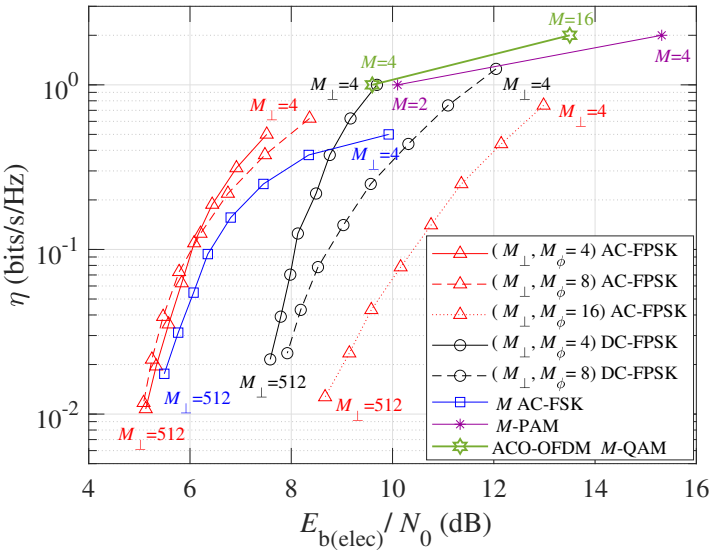

Figure 12: Simulated spectral efficiency η versus required $E_{\mathrm{b(elec)}}/N_0$ to achieve a BER $= 10^{-3}$ for $(M_\perp, M_\phi)$-AC-FPSK, M AC-FSK [20], $(M_\perp, M_\phi)$-DC-FPSK, M PAM [10] and ACO-OFDM M-QAM [5].

it is necessary to find out the optimal M_ϕ to achieve the best trade-off between energy efficiency and spectral efficiency. It is the purpose of the next section.

5.3. Spectral Efficiency versus Energy Efficiency Trade-off

Fig. 12 depicts the spectral efficiency, η versus the required $E_{\mathrm{b(elec)}}/N_0$ to achieve a BER $= 10^{-3}$ for $(M_\perp, M_\phi)$-AC-FPSK, M AC-FSK, $(M_\perp, M_\phi)$-DC-FPSK, M PAM and ACO-OFDM . Note that different M_ϕ and $M_\perp$ are considered for AC-FPSK and DC-FPSK, i.e., $M_\phi \in \{4, 8, 16\}$ and $M_\perp \in \{4, 8, 16, \cdots, 512\}$. The 2-tap harmonic receiver is used for AC-FPSK and AC-FSK [20] and the TD ML receiver is used for DC-FPSK [21] and M-PAM [19],[20]. It can be seen from Fig. 12 that, for a target spectral efficiency $\eta = 10^{-1}$ bit/s/Hz, ($M_\perp$, 4)-AC-FPSK requires 2 dB lower $E_{\mathrm{b(elec)}}/N_0$ as compared to ($M_\perp$, 4)-DC-FPSK to reach a BER of 10^{-3}. This is due to the DC offset added in DC-FPSK waveforms that significantly increases the symbol energy without increasing the minimum squared Euclidean distance, $d^2_{\min}$ between the waveforms [19]. Furthermore, it can be noticed from Fig. 12 that ($M_\perp$, 4)-AC-FPSK and ($M_\perp$, 8)-AC-FPSK have improved performance over conventional M AC-FSK (from 0.35 to 3 dB energy gain when η goes from 10^{-1} to 5×10^{-1} bit/s/Hz, and about 0.3 dB energy gain for $\eta < 10^{-1}$ bit/s/Hz). This is due to the increase of AC-FPSK spectral efficiency relatively to M AC-FSK (see Table 1) while the minimum squared Euclidean distance, $d^2_{\min}$ between AC-FPSK waveforms (11) is not strongly impacted when $M_\phi \leq 8$. However, for $M_\phi = 16$, ($M_\perp$, 16)-AC-FPSK shows significant degradation in performance relative to M AC-FSK due to the strong reduction of the minimum squared Euclidean distance between AC-FPSK waveforms, $d^2_{\min}$ (cf. Fig. 4) while the spectral efficiency is improved with a limited gain.

Table 2: Average electrical power and peak electrical power for M PPM and $(M_\perp, M_\phi)$-AC-FPSK (A being the waveform maximum amplitude) and related PAPR.

Modulation Scheme	$P_{(\text{elec})}$	$P_{(\text{elec})}^{\text{peak}}$	PAPR
M PPM	$\frac{A^2}{M}$	A^2	M
$(M_\perp, M_\phi)$-AC-FPSK	$\frac{A^2}{4}$	A^2	4

Finally, from Fig. 12, it can be concluded that the optimum number of phases, M_ϕ to reach the best spectral efficiency versus energy efficiency trade-off for AC-FPSK is $M_\phi = 4$ or $M_\phi = 8$, depending on $M_\perp$ (i.e., on the target spectral efficiency). $M_\phi = 8$ offers a marginal improvement in terms of spectral efficiency versus energy efficiency trade-off over $M_\phi = 4$; however it allows reducing $M_\perp$ by a factor of 2 for a given target $M = M_\perp \times M_\phi$. Since $M_\perp$ has a more significant weight in the harmonic receiver complexity than M_ϕ (cf. Fig. 9), $M_\phi = 8$ is a suitable choice to minimize the receiver complexity and to optimize the spectral efficiency versus energy efficiency trade-off. Moreover, the performances of the M PAM [10] and ACO-OFDM M-QAM [5] have also been reported in Fig. 12. The spectral efficiency of the M PAM and ACO-OFDM M-QAM is increasing with M [23], but the BER performances of M PAM and ACO-OFDM M-QAM are worse than the proposed $(M_\perp, M_\phi)$-AC-FPSK when targetting high energy efficiency at low spectral efficiency.

Considering $M_\phi = 4$ and $M = 512$, the complexity of the 2-tap harmonic receiver for $(M_\perp, 4)$-AC-FPSK is found to be 83.3% larger than the complexity of the 2-tap harmonic receiver for M AC-FSK [20], whereas considering $M_\phi = 8$ and for any M value, the complexity of the 2-tap harmonic receiver for $(M_\perp, 8)$-AC-FPSK is found to be strictly equal to the complexity of the 2-tap harmonic receiver for M AC-FSK.

5.4. Comparison of $(M_\perp, 8)$-AC-FPSK with pure orthogonal modulation (M PPM)

In practical environments, large PAPR modulations driving LEDs with limited dynamic range induce serious performance limitations [24]. Therefore, it is relevant to consider the peak energy per bit, $E_{\text{b(elec)}}^{\text{peak}}$, to evaluate the BER performance as a function of $E_{\text{b(elec)}}^{\text{peak}}/N_0$ metrics. According to [19], the peak electrical power, $P_{(\text{elec})}^{\text{peak}}$, and the average electrical power, $P_{(\text{elec})}$, are related as:

$$P_{(\text{elec})}^{\text{peak}} = \lambda_{(\text{elec})} P_{(\text{elec})}, \tag{23}$$

where $\lambda_{(\text{elec})}$ is the modulation PAPR whose values for M PPM and $(M_\perp, M_\phi)$-AC-FPSK are presented in Table 2. As a result, $E_{\text{b(elec)}}^{\text{peak}}/N_0$ can be evaluated as:

$$\frac{E_{\text{b(elec)}}^{\text{peak}}}{N_0} = \lambda_{(\text{elec})} \frac{E_{\text{b(elec)}}}{N_0}. \tag{24}$$

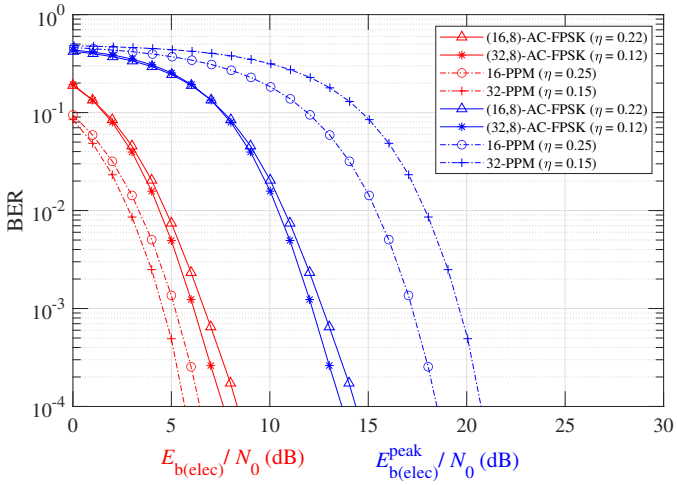

Figure 13: Simulated BER performance against $E_{\mathrm{b(elec)}}/N_0$ and $E^{\mathrm{peak}}_{\mathrm{b(elec)}}/N_0$ (limited dynamic range LED) for $(M_{\perp}, 8)$-AC-FPSK versus M PPM in AWGN channel, considering optimal TD ML receiver, $M_{\perp} = \{16, 32\}$.

where $E_{\mathrm{b(elec)}}$ is the average energy per bit. Fig. 13 illustrates the BER performance as a function of $E_{\mathrm{b(elec)}}/N_0$ (in red) and $E^{\mathrm{peak}}_{\mathrm{b(elec)}}/N_0$ (in blue) for the proposed $(M_{\perp}, 8)$-AC-FPSK and for pure orthogonal PPM modulation (i.e., M PPM) using optimal TD ML receiver, for almost similar spectral efficiencies (η). Large dictionary sizes have been considered for both PPM ($M \geq 16$) and AC-FPSK ($M \geq 128$) to target high energy efficiencies. From Fig. 13, it can be seen that M PPM shows around 1.5 dB better energy efficiency relative to $(M_{\perp}, 8)$-AC-FPSK at a BER $= 10^{-3}$ for the same spectral efficiency due to the perfect orthogonality between M PPM waveforms. However, considering LED dynamic range limitation with related $E^{\mathrm{peak}}_{\mathrm{b(elec)}}/N_0$ metrics, it is obvious from Fig. 13 that the BER performance of M PPM is significantly degraded comparatively to the case when no dynamic range limitation is included (i.e. $E_{\mathrm{b(elec)}}/N_0$ metrics) due to the large PAPR of PPM (PAPR $= M$ with $M \geq 16$, see Table 2). On the other hand, the BER performance of $(M_{\perp}, 8)$-AC-FPSK is also degraded but the energy efficiency penalty is lower than for M PPM due to a smaller PAPR value for $(M_{\perp}, 8)$-AC-FPSK (PAPR $= 4$, see Table 2). Interestingly, Fig. 13 also shows that, by increasing modulation order M, M PPM shows degraded energy efficiency when considering limited dynamic range LED (i.e. considering $E^{\mathrm{peak}}_{\mathrm{b(elec)}}/N_0$ metrics), despite the gain obtained from the orthogonal nature of the PPM modulation. This is due to the penalty induced by the PAPR of PPM, which increases linearly with M. On the other hand, since PAPR of $(M_{\perp}, 8)$-AC-FPSK is constant for any M, energy efficiency of $(M_{\perp}, 8)$-AC-FPSK is still improved by increasing M, even when considering limited dynamic range LED.

6. Conclusion

In this paper, we have proposed and analyzed $(M_\perp, M_\phi)$-AC-FPSK modulation scheme to address energy efficient OWC. It is based on aggregating asymmetrically-clipped FSK signaling with PSK modulation. Three different AC-FPSK receiver architectures have been proposed: the optimal TD ML receiver, the sub-optimal 1-tap DFT receiver, and the FD 2-tap harmonic receiver. The theoretical bounds for bit error probability, derived from minimum squared Euclidean distance analysis, are relatively close to the simulated BER results. Moreover, the 2-tap harmonic receiver for $(M_\perp, M_\phi)$-AC-FPSK attains similar performance as the TD ML receiver while showing a significantly reduced receiver complexity. Simulation results also reveal the optimum numbers of phases, $M_\phi = 4$ or 8, to obtain the best energy efficiency versus spectral efficiency trade-off compared to M AC-FSK and $(M_\perp, M_\phi)$-DC-FPSK modulation schemes. Actually, $M_\phi = 8$ is the best choice to lower the receiver complexity, reducing $M_\perp$ and then the DFT order for a given modulation size $M = M_\perp \times M_\phi$. Considering $M_\phi = 8$, the complexity of harmonic receiver is the same for $(M_\perp$, 8)-AC-FPSK and M AC-FSK, while $(M_\perp$, 8)-AC-FPSK shows improved spectral efficiency versus energy efficiency trade-off. $(M_\perp$,$M_\phi)$-AC-FPSK achieves better energy efficiency than usual linear M PAM modulation and ACO-OFDM. Additionally, $(M_\perp$,$M_\phi)$-AC-FPSK attains better energy efficiency as compared to pure orthogonal M PPM modulation when LED dynamic range limitation is taken into account. The advantages over classical approaches identified at this moment make $(M_\perp, M_\phi)$-AC-FPSK a good candidate for low-energy and low-data rate OWC.

An extension of this work may include: i) investigating the performance of $(M_\perp, M_\phi)$-AC-FPSK over a time-dispersive OWC channel, ii) providing experimental results to prove $(M_\perp, M_\phi)$-AC-FPSK modulation benefits under practical OWC scenario, and iii) investigating a joint modulation/coding approach to improve further the energy efficiency of the proposed modulation technique.

References

[1] Miqueu Paul, Khan Muhammad Jehangir, Le Guennec Yannis, and Ros Laurent. Turbo-DC-FPSK: A joint turbo coding and FPSK based modulation scheme adapted to optical wireless communications. In *2023 16th International Conference on Signal Processing and Communication System (ICSPCS)*, pages 1–7, 2023.

[2] Lin Zhang, Ying-Chang Liang, and Ming Xiao. Spectrum sharing for internet of things: A survey. *IEEE Wireless Communications.*, 26(3):132–139, 2019.

[3] H. Haas, C. Chen, and D. O'Brien. A guide to wireless networking by light. *Progress in Quantum Electronics.*, 55:88–111, 2017.

[4] Mostafa Zaman Chowdhury, Moh. Khalid Hasan, Md. Shahjalal, Md. Tanvir Hossan, and Yeong Min Jang. Optical wireless hybrid networks: Trends, opportunities, challenges, and research directions. *IEEE Communications Surveys & Tutorials.*, 22(2):930–966, 2020.

[5] Sarangi D. Dissanayake, Kusha Panta, and Jean Armstrong. A novel technique to simultaneously transmit ACO-OFDM and DCO-OFDM in IM/DD systems. In *2011 IEEE GLOBECOM Workshops (GC Wkshps)*, pages 782–786, 2011.

[6] Simeng Feng, Qihui Wu, Chao Dong, and Baolong Li. A spectrum enhanced ACO-OFDM scheme for optical wireless communications. *IEEE Communications Letters.*, 27(2):581–585, 2023.

[7] Yaqi Sun, Fang Yang, and Ling Cheng. An overview of OFDM-based visible light communication systems from the perspective of energy efficiency versus spectral efficiency. *IEEE Access.*, 6:60824–60833, 2018.

[8] M.-A. Khalighi, S. Long, S. Bourennane, and Z. Ghassemlooy. PAM-and CAP-based transmission schemes for visible-light communications. *IEEE Access.*, 5:27002–27013, 2017.

[9] Asanka Nuwanpriya, Siu-Wai Ho, Jian Andrew Zhang, Alex J Grant, and Lin Luo. PAM-SCFDE for optical wireless communications. *Journal of Lightwave Technology.*, 33(14):2938–2949, 2015.

[10] John G. Proakis and Masoud Salehi. *Digital communications*. McGraw-Hill, 5th edition, 2008.

[11] Yoann Roth, Jean-Baptiste Doré, Laurent Ros, and Vincent Berg. The Physical Layer of Low Power Wide Area Networks: Strategies, Information Theory's Limit and Existing Solutions. In *Advances in Signal Processing: Reviews, Vol. 1, Book Series*. August 2018.

[12] Xiaoxue Ma, Kyujin Lee, and Kyesan Lee. Appropriate modulation scheme for visible light communication systems considering illumination. *Electronics letters.*, 48(18):1137–1139, 2012.

[13] Taissir Youssef Elganimi. Performance comparison between OOK, PPM and PAM modulation schemes for free space optical (FSO) communication systems: analytical study. *International Journal of Computer Applications.*, 79(11), 2013.

[14] Angga Pradana, Nur Ahmadi, Trio Adiono, Willy Anugrah Cahyadi, and Yeon-Ho Chung. VLC physical layer design based on pulse position modulation (PPM) for stable illumination. In *2015 International Symposium on Intelligent Signal Processing and Communication Systems (ISPACS)*, pages 368–373. IEEE, 2015.

[15] CT Manimegalai, Sabitha Gauni, Nikita Raghavan, and T Rama Rao. Investigations on suitable modulation techniques for visible light communications. In *2017 International Conference on Wireless Communications, Signal Processing and Networking (WiSPNET)*, pages 1818–1822. IEEE, 2017.

[16] G.M Mougoue Yamga, A. R. Ndjiongue, and K. Ouahada. Low complexity clipped frequency shift keying (FSK) for visible light communications. In *2018 IEEE 7th International Conference on Adaptive Science & Technology (ICAST)*, pages 1–6, 2018.

[17] Marlon Lucas Gomes Salmento, Guilherme Marcio Soares, Jose Marcos Alonso, and Henrique A. C. Braga. A dimmable offline LED driver with OOK-M-FSK modulation for VLC applications. *IEEE Transactions on Industrial Electronics.*, 66(7):5220–5230, 2019.

[18] Cristobal Guajardo-Penroz, Ismael Soto, Enrique San-Juan, Pablo Adasme, Cesar Azurdia-Meza, and Wilson Alavia. New high dimming range M-FSK demodulation strategy for VLC systems. In *2020 12th International Symposium on Communication Systems, Networks and Digital Signal Processing (CSNDSP)*, pages 1–6, 2020.

[19] Ali Waqar Azim, Antoine Rullier, Yannis Le Guennec, Laurent Ros, and Ghislaine Maury. Energy efficient M-ary Frequency-Shift Keying-based modulation techniques for visible light communication. *IEEE Transactions on Cognitive Communications and Networking.*, 5(4):1244–1256, 2019.

[20] Muhammad Jehangir Khan, Ali Waqar Azim, Yannis Le Guennec, Ghislaine Maury, and Laurent Ros. Asymmetrically clipped-FSK modulation for energy efficient visible light communications. In *2021 IEEE 32nd Annual International Symposium on Personal, Indoor and Mobile Radio Communications (PIMRC)*, pages 458–464. IEEE, 2021.

[21] Ali Waqar Azim, Yannis Le Guennec, and Laurent Ros. Hybrid frequency and phase-shift keying modulation for energy efficient optical wireless systems. *IEEE wireless communications letters.*, 9(4):429–432, 2019.

[22] Muhammad Jehangir Khan, Ali W Azim, Yannis Le Guennec, Ghislaine Maury, and Laurent Ros. Theoretical and experimental analysis of Asymmetrically Clipped-FSK VLC system. *IEEE Photonics Journal.*, 14(3):1–9, 2022.

[23] Zabih Ghassemlooy, Wasiu Popoola, and Sujan Rajbhandari. *Optical wireless communications: system and channel modelling with Matlab®*. CRC press, Boca Raton, 2019.

[24] Hany Elgala, Raed Mesleh, and Harald Haas. A study of LED nonlinearity effects on optical wireless transmission using OFDM. In *2009 IFIP International Conference on Wireless and Optical Communications Networks*, pages 1–5. IEEE, 2009.